Hindawi Publishing Corporation
Journal of Nanomaterials
Volume 2008, Article ID 132728, 11 pages
doi:10.1155/2008/132728

Research Article

Buckling of Single-Crystal Silicon Nanolines under Indentation

Min K. Kang,[1] Bin Li,[2] Paul S. Ho,[2] and Rui Huang[1]

[1] *Department of Aerospace Engineering and Engineering Mechanics, University of Texas, Austin, TX 78712, USA*
[2] *Microelectronics Research Center, University of Texas, Austin, TX 78758, USA*

Correspondence should be addressed to Rui Huang, ruihuang@mail.utexas.edu

Received 1 October 2007; Accepted 27 December 2007

Recommended by Junlan Wang

Atomic force microscope-(AFM-) based indentation tests were performed to examine mechanical properties of parallel single-crystal silicon nanolines (SiNLs) of sub-100-nm line width, fabricated by a process combining electron-beam lithography and anisotropic wet etching. The SiNLs have straight and nearly atomically flat sidewalls, and the cross-section is almost perfectly rectangular with uniform width and height along the longitudinal direction. The measured load-displacement curves from the indentation tests show an instability with large displacement bursts at a critical load ranging from 480 μN to 700 μN. This phenomenon is attributed to a transition of the buckling mode of the SiNLs under indentation. Using a set of finite element models with postbuckling analyses, we analyze the indentation-induced buckling modes and investigate the effects of tip location, contact friction, and substrate deformation on the critical load of mode transition. The results demonstrate a unique approach for the study of nanomaterials and patterned nanostructures via a combination of experiments and modeling.

Copyright © 2008 Min K. Kang et al. This is an open access article distributed under the Creative Commons Attribution License, which permits unrestricted use, distribution, and reproduction in any medium, provided the original work is properly cited.

1. INTRODUCTION

Silicon (Si)-based nanomaterials [1–9] have drawn much attentionrecently due to continual miniaturization of semiconductor devices in microelectronics and development of nanoelectromechanical systems (NEMSs). One of the persisting challenges for practical applications of nanomaterials has been the measurement of their mechanical properties, which as well known can be different from their counterparts of bulk materials. A variety of metrology methodologies have been developed, such as nanoscale tensile tests [10–12], resonance methods [13, 14], bending techniques [1, 2, 4–6], and nanoindentation tests [7, 15]. In particular, the nanoindentation tests have been well established for measuring mechanical properties such as elastic modulus, hardness, and fracture toughness, for both bulk and thin-film materials [16, 17], with very high force/displacement resolution and excellent controllability. Recently, the nanoindentation technique has been adopted for mechanical characterization of various nanomaterials [15], including nanotubes [18, 19], nanowires [20, 21], nanobelts [22], and nanoparticles [7]. However, interpretation of the nanoindentation results for nanomaterials is nontrivial and often requires sophisticated modeling effort [7, 21, 23, 24].

In this paper, we carry out nanoindentation experiments to characterize the mechanical properties of single-crystal Si nanolines (SiNLs). These SiNLs are fabricated by a process combining electron beam lithography (EBL) and anisotropic wet etching [25, 26]. They have atomically flat sidewalls and almost perfectly rectangular cross sections. The measured indentation load-displacement curves show a peculiar character with a large displacement burst at a critical load. A finite element model is developed to simulate the indentation test, which reveals a buckling mechanism of the SiNLs under indentation. A systematic modeling effort is presented here to elucidate the effects of the indenter tip location, contact friction, and substrate deformation on the critical load. The results demonstrate a potential methodology to study buckling, friction, and fracture of nanomaterials through a combination of experiments and modeling.

2. EXPERIMENTAL

Figure 1 shows an array of parallel SiNLs fabricated by a process combining EBL and anisotropic wet etching. The fabrication process began with chemical vapor deposition of an oxide layer on a Si (110) wafer, followed by depositing

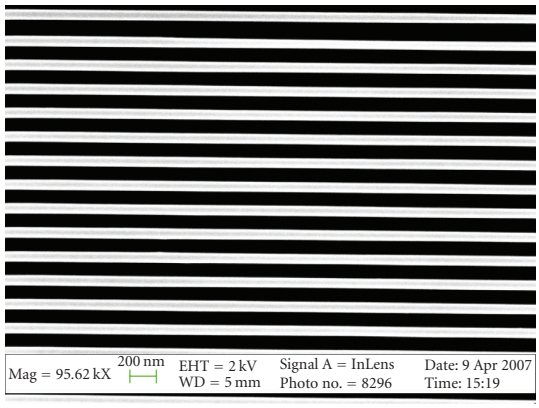

(a)

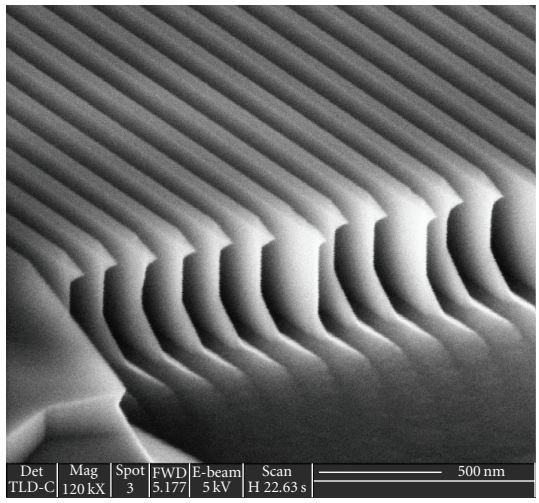

(b)

Figure 1: SEM images of parallel silicon nanolines, with 74 nm line width and 510 nm height; the pitch distance is 180 nm. (a) A plan view, (b) a perspective view with 60° tilt angle. A trench pattern is specially designed at one end of the line for the SEM image in (b), showing the cross sections of the nanolines with sharp edges due to anisotropic etching.

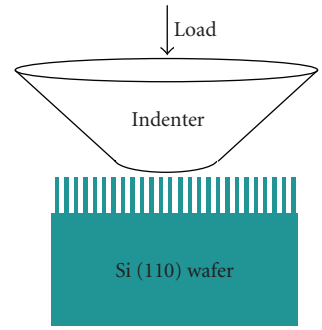

(a)

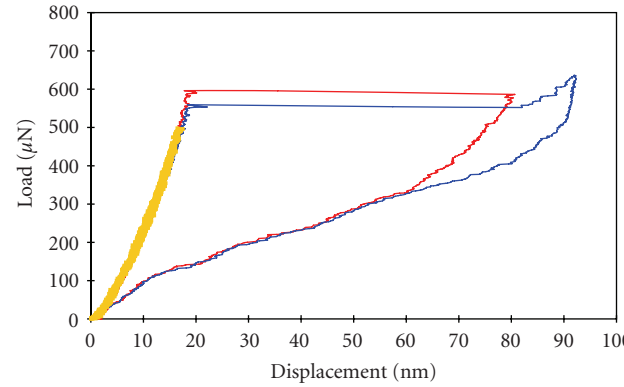

(b)

Figure 2: (a) Schematic of the nanoindentation test on parallel SiNLs. (b) A set of three load-displacement curves from the nanoindentation tests on the 74 nm SiNLs, with no residual deformation after unloading of the indenter.

a thin chromium layer. A positive photoresist was then spun on the wafer and patterned using an electron beam exposure system.Pattern transfer from the resist was performed by plasma etching of the chromiumand oxide down to the silicon surface. Subsequently, the residual resist was removed and tetra-methyl-ammonium hydroxide (TMAH) was used for anisotropic etching of the Si,with the remaining chromium and oxide layers as the hard mask. When the EBL patterned lines were aligned with one of the ⟨112⟩ directions on the Si surface, parallel SiNLs were produced by the anisotropic etchingalong the {111} crystalline planes, with vertical and atomically flat sidewalls. Finally, the residual chromium and oxide were removed by chromium etchant and bufferedoxide etchant (BOE), respectively. Figure 1(a) shows highly uniform line width along the longitudinal directions of the SiNLs, and Figure 1(b) shows a perspective view near one end of the SiNLs where a trench pattern was specially designed for the purpose of SEM imaging. The line width of the SiNLs shown in Figure 1 is 74 nm, and the height is 510 nm, corresponding to an aspect ratio of 6.9 for the rectangular cross section. The pitch distance is 180 nm. Following the same process, we have successfully fabricated SiNLs with line widths ranging from 40 nm to 500 nm. The height of the SiNLs can be controlled by TMAH etching time within the range of 100–2000 nm, and the length is defined by the exposed area for electron-beam patterning, which was 50 μm for the present study. The high crystal quality and well-defined line geometry, along with the atomically flat sidewalls and highly uniform line width, make these SiNLs well suited for accurate experimental measurements and modeling.

An atomic force microscope (AFM)-based nanoindentation system (Triboscope by Hysitron, Inc.) was used to characterize the mechanical properties of the SiNLs. A conically shaped diamond indenter with the tip radius around 5 μm was used to probe the SiNLs, as schematically illustrated in Figure 2(a). The tip radius was more precisely determined by scanning electron microscope (SEM) to be 4.6 μm. During each indentation test, the indenter was placed directly above an array of parallel SiNLs, patterned in a 50 μm by 50 μm area of the wafer surface. The indenter was

brought into contact with the SiNLs, monitored by a build-in transducer. Subsequently, loading and unloading of the indenter were performed with the force and displacement measured simultaneously. Figure 2(b) shows three load-displacement curves obtained from the indentation tests on the 74 nm SiNLs. In the first test (thick yellow curve in the plot), a small indentation load of 500 μN was applied and subsequently unloaded, which shows an elastic response with coinciding curves for loading and unloading. With the indentation load increased beyond 550 μN for the second and third tests, a large displacement burst was observed. This indicates the occurrence of instability under indentation. Similar displacement bursts were observed in nanoindentation experiments of metal films, which were attributed to a dislocation mechanism as an intrinsic material instability [24]. Here, however, the magnitude of the displacement burst is much larger (over 60 nm in comparison with a few nanometers for the metal films). As noted in a previous study [2], plastic deformation of nanoscale single-crystal Si beams was observed only at elevated temperatures (> 373 K), thus the dislocation mechanism is not expected to operate at the room temperature. Furthermore, it was found that, after the displacement burst, unloading of the indenter fully recovers the displacement, with no observable residual deformation. This suggests a likely instability mechanism due to buckling of the SiNLs, to be confirmed by modeling simulations as discussed in the later sections.

Additional indentation tests with the SiNLs were carried out with various indentation loads, as shown in Figure 3(a). Here, however, irrecoverable residual deformation was observed after unloading of the indenter. It is noted that the maximum indentation displacement for each of these tests is greater than 150 nm, while in Figure 2(a) the maximum displacement was less than 100 nm. It is thus conjectured that the larger indentation displacements in this set caused more significant bending of the SiNLs after the buckling instability, which in turn induced higher tensile stresses that eventually fractured the SiNLs. Indeed, debris of fractured Si were observed, as shown in Figure 3(b) for one of these tests. Remarkably, the debris of the fractured SiNLs are of isosceles triangular shape, with two sides well aligned in the $\langle 110 \rangle$ directions and the base in the $\langle 112 \rangle$ direction parallel to the SiNLs. This indicates a primary cleavage mechanism of the close packed $\{111\}$ planes along the $\langle 110 \rangle$ directions [17]. This opens a possibility to study fracture of Si at the nanoscale.

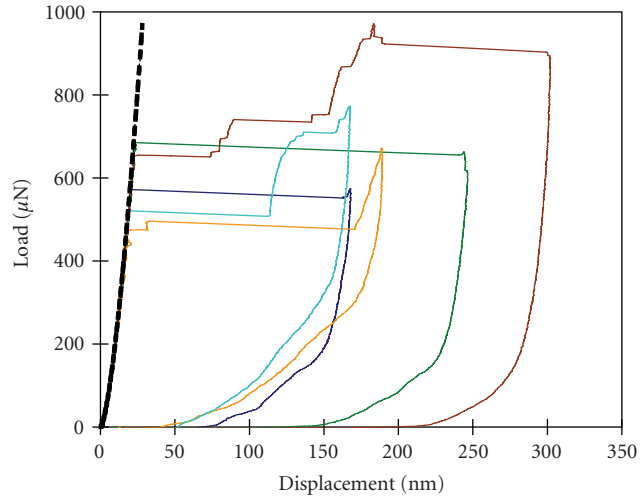

(a)

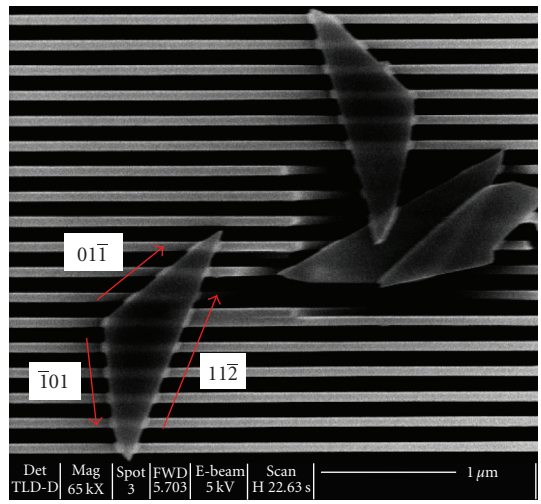

(b)

Figure 3: (a) A set of five load-displacement curves from the nanoindentation tests on the 74 nm SiNLs, with irrecoverable displacements due to fracture of the SiNLs. (b) A SEM image of the fractured SiNLs, with debris of isosceles triangular shape.

3. FINITE ELEMENT MODEL

In this section,we calibrate a finite element model to simulate the nanoindentation test on SiNLs. The model system consists of a spherical indenter and parallel SiNLs standing on a substrate, as illustrated in Figure 4. Since the tip radius ($R = 4.6\,\mu$m) is much greater than the line width ($w = 74$ nm) and the pitch ($S = 180$ nm), the conical indenter used in the experiments is effectively modeled by the spherical indenter of the same tip radius. Furthermore, the indenter is modeled as a rigid body. This approximation is justified by noting that Young's modulus of the diamond indenter (1140 GPa) is much greater than that of Si (e.g., 169 GPa in the [110] direction). It was confirmed that a similar model with an elastic diamond indenter predicts a load-displacement curve nearly identical to the rigid indenter model, as shown in Figure 5. On the other hand, the elastic indenter model requires significantly higher computational effort, with a larger number of elements, especially for the contact between the indenter and the SiNLs. Next, the Si substrate is modeled as a rigid foundation to the SiNLs. This approximation is made by considering that the patterned SiNLs, with air gaps in between, are more compliant than the solid substrate. The effect of elastic deformation in the substrate will be further discussed in the next section. Finally, the material of SiNLs is assumed to be linearly elastic and isotropic. As suggested by Vlassak et al. [27], modeling indentation on

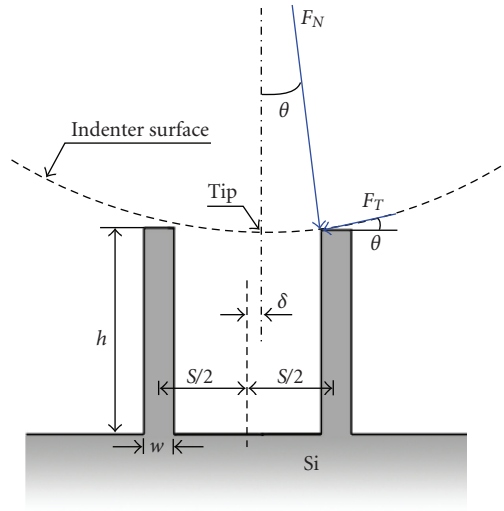

Figure 4: Illustration of the parallel SiNLs under spherical indentation (not to the scale), showing the cross sections of two lines and the contact forces. The tip alignment is indicated by an offset δ from the trench center.

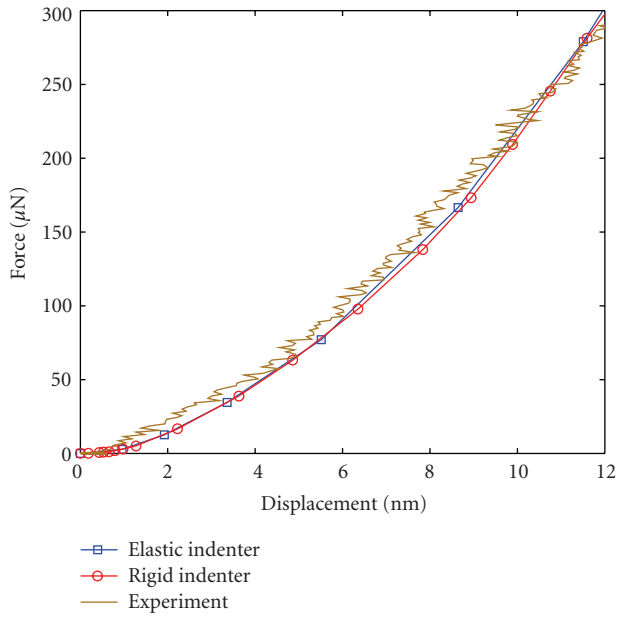

Figure 5: Calibration of the finite element model using the experimental data. The elastic indenter model and the rigid indenter model give nearly identical load-displacement curves, both in good agreement with the experimental data.

elastically anisotropic materials can be simplified by using an equivalent isotropic model. To determine the equivalent isotropic elastic modulus for the SiNLs, we compare the load-displacement curve obtained from the model to the experimental curves shown in Figure 2(b). With the Poisson's ratio fixed as 0.27, we found that a Young's modulus of 140 GPa gives a load-displacement curve in good agreement with the experimental curve, as shown in Figure 5. This

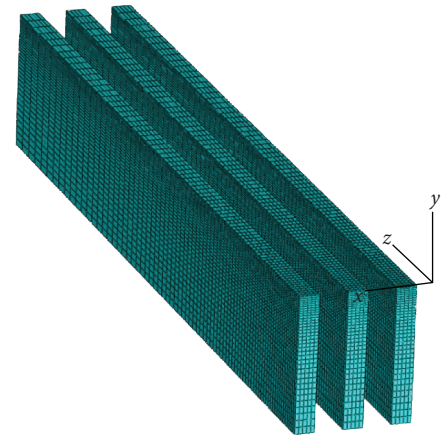

Figure 6: A finite element model of parallel SiNLs under indentation, showing three half-lines with symmetric boundary conditions at the planes $z = 0$ and $x = 0$. The tip of the indenter moves along the y-axis during the simulation for a symmetric trench-center loading.

modulus is lower than the Young's modulus of bulk Si in the [110] direction, but higher than that in the [001] direction.

Three-dimensional finite element (FE) models are constructed for the SiNLs using ABAQUS [28]. Figure 6 shows an example model, with the tip of the indenter aligned with a trench center (i.e., $\delta = 0$ in Figure 4). By symmetry, three half-lines on one side of the tip are modeled for indentation on six parallel SiNLs. The number of lines and the indenter tip location are varied to investigate their effects, as discussed in the next section. The length of the SiNLs in the experiments was 50 μm, much greater than the line width ($w = 74$ nm) and height ($h = 510$ nm). In the FE model, the lines are 6 μm long. The length is chosen such that the boundary condition at the ends has negligible effect on the simulation results, mimicking infinitely long lines. Only half of each line is modeled, with a symmetry boundary condition for the cross section at $z = 0$.

To model the indentation load, contact surfaces are defined between the indenter and the lines. The contact property, either frictionless or frictional, is specified. As discussed in the next section, the friction between the indenter tip and the SiNLs is very important in determining the critical buckling load. On the other hand, contact and friction among SiNLs are ignored because of the relatively large spacing between the lines ($S/w > 2$). For columnar structures with narrow spacing such as those in thermal barrier coatings [28, 29], the inter-columnar contact and friction are critical. To simulate buckling and post-buckling behavior of the SiNLs, the modified Riks method [30, 31] is adopted for the FE simulations. The essence of the Riks method is that the solution is viewed as a single equilibrium path in a space defined by both the nodal displacements and the loading parameters. This approach solves simultaneously for loads and displacements, thus providing solutions regardless of whether the response is stable or unstable. The contact between the indenter and the lines and possible loss of the contact in the present model often causes divergence in the numerical simulations. A spring-dashpot element

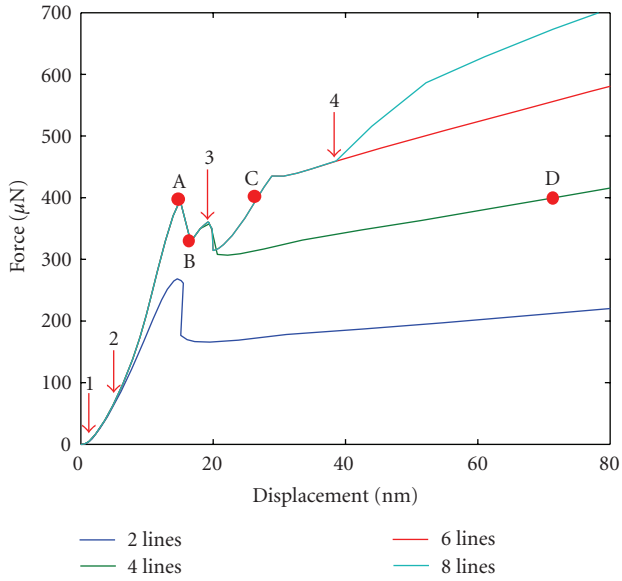

FIGURE 7: Indentation load-displacement curves from finite element models with different numbers of lines. The indenter tip is aligned with the trench center between two center lines. The initiation of contact with the first four pairs of the lines is indicated by the arrows with numbers 1–4.

[30] has been used as a numerical damper to stabilize the numerical simulations, which effectively adjusts the step size to relieve the sudden force change upon contact and buckle initiation.

4. RESULTS AND DISCUSSIONS

4.1. *Symmetric loading with frictionless contact*

We begin with a simplest model, assuming frictionless contact between the indenter and the lines. The tip of the indenter is aligned with a trench center between two lines (i.e., $\delta = 0$ in Figure 4). The number of lines in the model is varied from 2 to 8 by including the neighboring lines, all placed symmetrically with respect to the tip location. The condition of symmetry is used to reduce the number of elements and thus the computational time. Figure 7 plots the indentation load-displacement curves from the FE simulations. By comparing the curves for different numbers of lines, we can determine the initiation of multiple contacts at different indentation depths,as indicated by the vertical arrows in Figure 7. The first contact occurs between the indenter and the two center lines, with a very small displacement of the tip from its initial position at the same height as the lines. The indentation force is zero before the first contact and increases with the tip displacement afterwards. This part is the same for all the curves, as the first contact occurs in all the four models. The curve for the two-line model deviates from the other curves after the tip displacement reaches 5.9 nm, at which point the indenter makes contact with the next pair of lines adjacent to the center lines. This second contact is absent in the two-line model, which gives a more compliant force-displacement curve thereafter. Similarly, the curve of the four-line model deviates from the other two after the third contact at the tip displacement of 18.6 nm, and the six-line curve deviates from the eight-line curve after the fourth contact at the tip displacements of 38.4 nm. The tip displacements for the initiation of each contact can be confirmed from a pure geometric consideration using the given radius of the rigid spherical indenter along with the line width and the pitch distance.

All the force-displacement curves in Figure 7 exhibit an unstable behavior, with the force decreasing after a critical load. While the critical load for the two-line model is significantly lower, the other three models give the same critical load, as the instability occurs after the second contact but before the third contact. In other words, at the critical load, only the four lines nearest to the tip of the indenter are in contact and thus subject to the contact forces. The detail of the instability is elucidated by the six-line model in Figure 8. Figure 8(a) shows the deformation of the SiNLs and the stress distribution immediately before the instability, indicated as point A on the load-displacement curve (see Figure 7). At this point, the center two lines are bent symmetrically, with the cross section taking a half-wave shape and nearly perpendicular to the surface of the indenter at the contact. This is similar to the buckling mode of a column with one end fixed and the other end constrained of rotation (see the inset). Apparently, the frictionless contact allows lateral sliding of the lines along the spherical surface, but the compressing rigid surface constrained the rotation of the top surface of the lines. Such constraint however is lost in Figure 8(b), corresponding to point B on the load-displacement curve (see Figure 7). Now, the cross section of the center two lines takes a quarter-wave shape, similar to the buckling mode of a column with one end fixed and the other end free of any constraint (see the inset). The transition of the buckling mode is thus responsible for the instability shown in Figure 7. The quarter-wave mode is more compliant (less constrained) than the half-wave mode, leading to the force drop from A to B in the load-displacement curve. Meanwhile, the next two lines are still bent in a half-wave mode at point B. A similar transition of the buckling mode for these two lines gives the second peak in the load-displacement curve. After that, all four lines nearest to the indenter tip are bent in the quarter-wave mode, as shown in Figure 8(c). It can be seen that the transition of the buckling mode is accompanied by significant sliding and partial loss of the contact between the indenter and the SiNLs.

While the Riks method used in the numerical simulation gives a single equilibrium path for each model, experimental curves depend on the control of the load or displacement. If the experiments were under a displacement control, similar curves as shown in Figure 7 would be expected. Under a load control, however, the equilibrium path in Figure 7 would predict a displacement burst at the critical load, that is, from point A to point C for the six-line model. This qualitatively agrees with the experimental curves shown in Figure 2(b). However, it is noted that, for models with six or more lines, the displacement burst starts at point A with only four lines in contact with the indenter but stops at

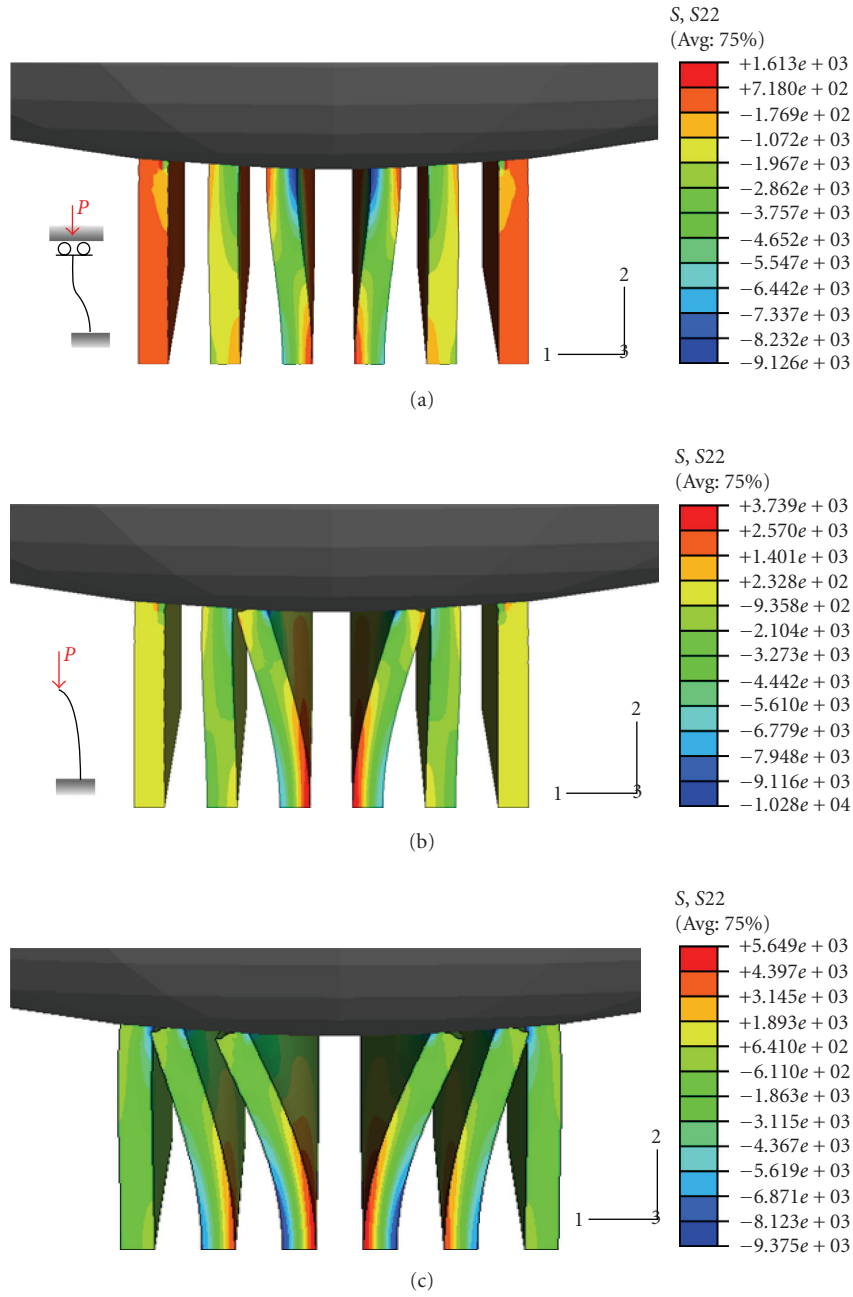

Figure 8: Buckling of SiNLs and mode transition simulated by the finite element model. The contours show the distributions of normal stress in the 2-direction. (a)–(c) correspond to the points A, B, C on the load-displacement curve in Figure 7, respectively. The insets in (a) and (b) show analogous buckling modes in columns.

point C with six lines in contact. This implies a possible dynamic contact process during the displacement burst, not captured in the present static analysis. This may account for the quantitative discrepancy in terms of the magnitude of the displacement jump between the experimental curves in Figure 2(b) and the equilibrium path in Figure 7. The former shows displacement jumps of over 60 nm, but the latter predicts only about 10 nm for the simulations with six or eight lines. Interestingly, a much larger displacement burst is predicted by the four-line model, about 55 nm from A to D. Apparently, the postbuckling behavior under the load-control experiments is complicated by the dynamic contact and friction processes, which is beyond the present static model and will be left for further investigations. In the present study, we focus on the critical load for the onset of the displacement burst, for which the static analysis of the present model suffices. Figure 7 shows that a minimum of four lines is sufficient for the modeling of the indentation test up to the critical load, because the contact with additional lines occurs only afterwards. The modeling however predicts

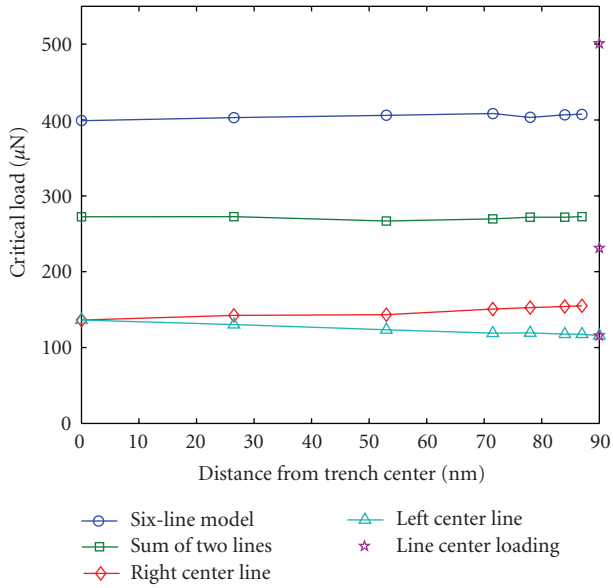

FIGURE 9: The critical load of buckling transition versus the indenter tip location, obtained from the finite element models. The critical loads for the left and right center lines are obtained from a single-line model.

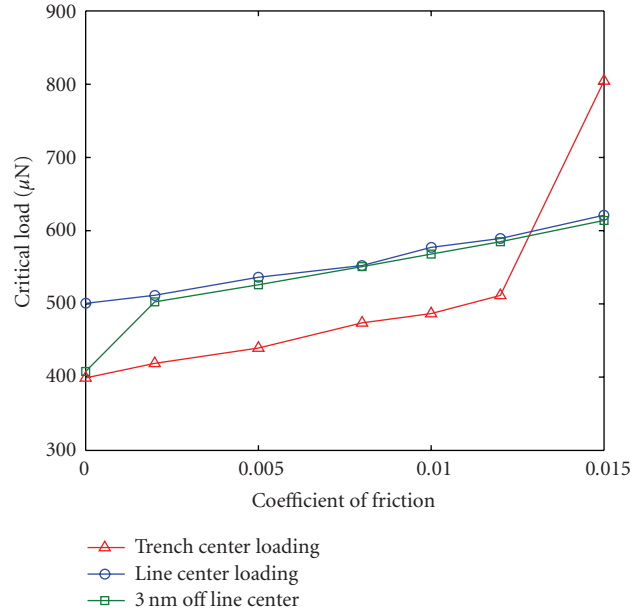

FIGURE 10: The critical load of buckling transition as a function of the friction coefficient at the contact, obtained from the finite element models with tip locations at the trench center, line center, and 3 nm off the line center.

a relatively low critical load at about 400 μN, while the critical load from the experimental curves (see Figures 2(b) and 3(a)) ranges from 480 μN to 700 μN. In the following, we discuss possible causes of this discrepancy by analyzing the effects of relative tip location, contact friction, and elastic deformation of the substrate.

4.2. *Effect of tip location*

The indentation tests of the present study were not equipped with sufficient lateral resolution for accurate positioning of the indenter with respect to individual SiNLs. The possible location of the indenter tip therefore could vary from a trench center between two lines to the center of one line (another case of symmetric loading). As illustrated in Figure 4, the eccentricity from the trench center, δ, varies from 0 to $S/2$, with S being the pitch distance between two adjacent lines. Figure 9 plots the critical load as a function of δ from the FE model with six lines. For the cases of asymmetric loading, six half-lines are meshed with one symmetric plane at $z = 0$ (refer to the coordinates in Figure 6). The contact between the indenter and the lines remains frictionless for the time being. It is found that shifting the relative tip location has negligible influence on the initial elastic response and the critical load. The no-effect on the elastic response before the critical load may be understood by noting the fact that the radius of the indenter is significantly larger than the pitch distance, and thus the variation of the contacts due to a shift of the tip location within the pitch distance is hardly noticeable by the large indenter. This is consistent with the experimental curves that follow a nearly identical path up to the critical load despite the uncertainty of the tip locations. On the other hand, the contact forces acting on each individual line vary asymmetrically with the tip location. For the center two lines that contribute the most to the total indentation force, the contact force is higher on the line closer to the tip and lower on the other one. Meanwhile, the critical load for each of these lines also varies with the tip location. As the tip moves closer (or farther) to the line, the contact angle θ decreases (or increases), and the critical load for the buckling mode transition of the individual line increases (or decreases). This trend has been confirmed by FE simulations with only one line under the indenter. Consequently, as the tip location shifts from the trench center towards the right side, the critical load increases for the right center lines but decreases for the left center line, as shown in Figure 9. Together with the redistribution of the contact forces on each line, the buckling instability occurs almost simultaneously for the two center lines, and the sum of the two individual critical loads is nearly independent of the tip location. The contact forces acting on the next two lines farther away from the tip account for the difference between the sum of the single-line critical loads and the total critical loads, also nearly independent of the tip location as a result of similar force redistribution.

As a special case, when the tip of the indenter is aligned exactly with the line center (i.e., $\delta = S/2$), the line directly underneath the tip is subjected to pure compression and does not buckle at all. In this case, the critical load is 500 μN, considerably higher than those for tip locations off the line center, as noted in Figure 9. A large portion of this critical load is due to the pure compression of the center line, while the buckling instability occurs for the two lines immediately adjacent to the center line. From a single-line model with the

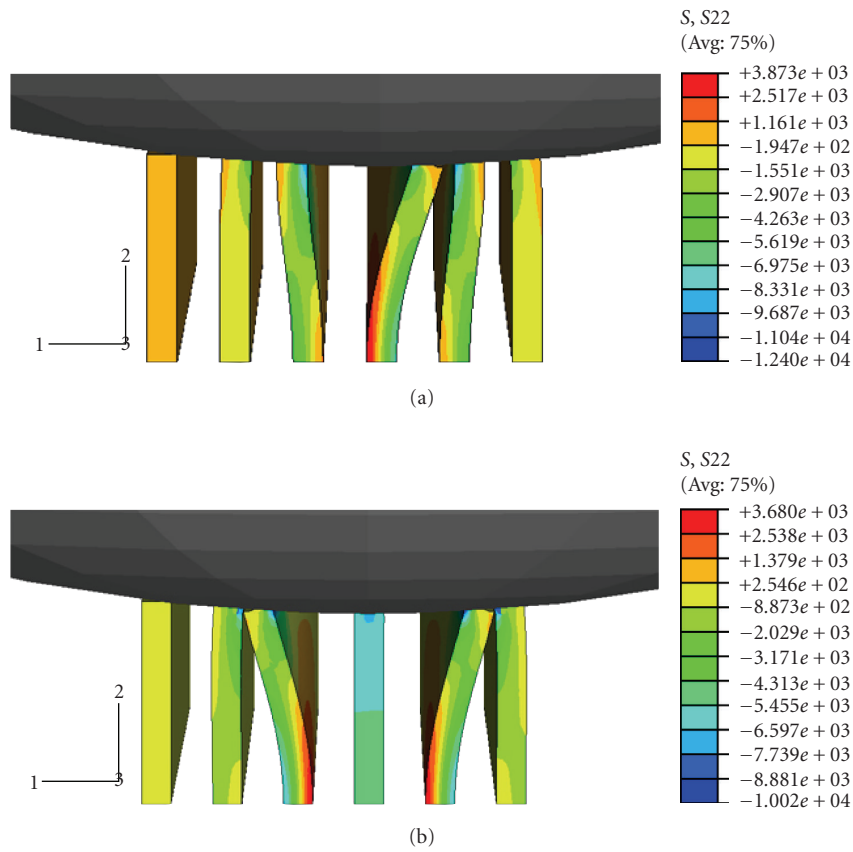

Figure 11: Simulated buckling modes of SiNLs under indentation with the indenter tip aligned 3 nm off the line center. (a) With frictionless contact between the indenter and the lines, (b) with coefficient of friction, $\mu = 0.002$, at the contact.

indenter tip located 180 nm off the line center (or, $\delta = 90$ nm for the left center line), the critical load for each of these two lines is obtained as 116 μN, twice of which contributes less than half of the total critical load from the six-line model.

4.3. Effect of friction

As illustrated in Figure 4, the normal contact force acting on the line tends to push the top of the line sliding against the indenter surface. This has been confirmed by the FE simulations assuming frictionless contact between the indenter and the SiNLs (see Figure 8). With friction, however, the sliding would be hindered, and thus the response of the SiNLs under indentation would be altered. By using a simple Coulomb friction model [28], we define a frictional contact surface between the indenter and the SiNLs in the FE models to analyze the effect of the friction coefficient μ. First, it is noted that the frictional contact property has negligible influence on the load-displacement curve before the critical load, for the coefficients of friction between 0 and 0.02 used in the present study. On the other hand, the critical load for the buckling transition of the SiNLs increases with the friction coefficient, as shown in Figure 10. With the indenter tip aligned at the trench center, the critical load increases from 400 μN for frictionless contact to about 510 μN with a friction coefficient $\mu = 0.012$. Clearly, the friction delays the transition of the buckling model that requires significant sliding of the contact surfaces. Further increasing the friction coefficient to 0.015 sees a sudden jump of the critical load to over 800 μN. This happens because of a change in the scenario. As the sliding of the center two lines is highly constrained by the frictional force, the transition of buckling mode occurs with the next two lines farther away from the tip while the center two lines are locked underneath the indenter without buckling. The total critical load in this case thus includes a large portion from the compression of the center two lines, plus the critical load for the next two lines. It is noted that the initial contact angle between the indenter and the center lines is about 0.0115, close to the coefficient of friction that locks down the sliding of the center line. For the next two lines, the initial contact angle is around 0.05, which requires a much larger coefficient of friction to lock down their sliding.

When the indenter tip is aligned with the line center, higher critical loads are obtained except for the case with the large friction coefficient $\mu = 0.015$, as shown in Figure 10. As discussed for the frictionless contact, with the perfect alignment, the center line is under pure compression and does not buckle. The friction then delays the transition of the buckling mode for the two lines closest to the center line,

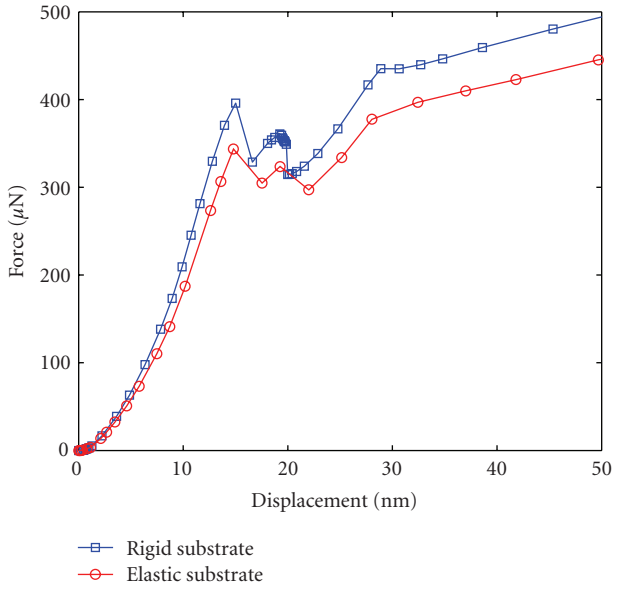

FIGURE 12: A comparison of indentation load-displacement curves from the finite element models of parallel SiNLs on a rigid substrate and on an elastic substrate, respectively.

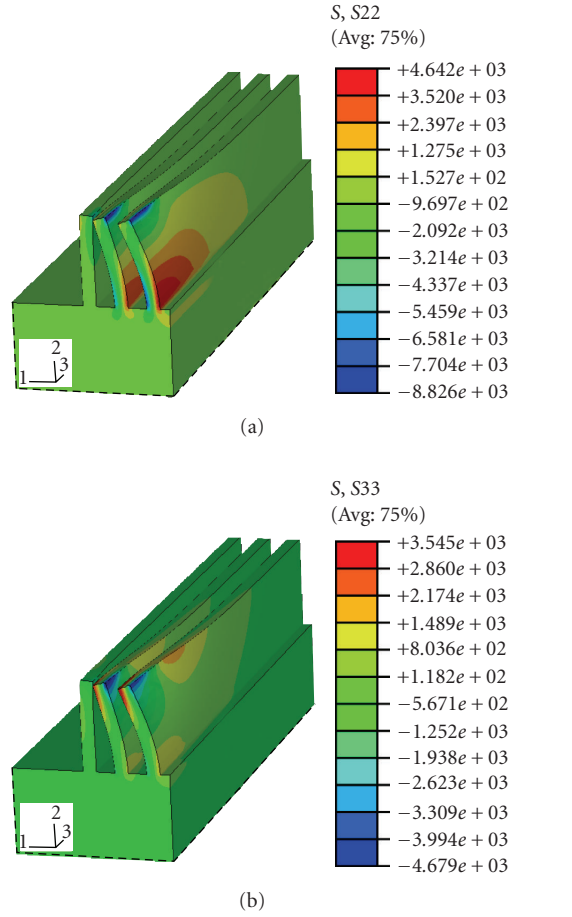

FIGURE 13: Stress distributions from a finite element model with SiNLs on an elastic substrate under a symmetric trench center loading. (a) and (b) show contours of the normal stresses in the 2- and 3-directions, respectively.

giving higher critical loads for larger coefficients of friction. For the case of the large friction coefficient ($\mu = 0.015$), the critical load for the line center indentation becomes lower than that for the trench center indentation, because the former has only one line locked underneath the indenter while the latter has two. Interestingly, when the location of the indenter tip is slightly off the line center, the center line can still be locked by the frictional contact, while it always slides and buckles with a frictionless contact. This is illustrated in Figure 11, which shows buckling of the SiNLs from the FE models with the indenter tip aligned 3 nm off the line center, one with frictionless contact and the other with a coefficient of friction $\mu = 0.002$. As shown in Figure 10, the former gives a critical load close to that under the symmetric trench-center loading, and the latter gives a critical load close to that under the exact line-center loading for the same coefficient of friction. Therefore, the friction at the contact leads to a change in the critical load and its dependence on the tip location.

The critical loads from the experiments, ranging from 480 μN to 700 μN, fall within the range shown in Figure 10 from the FE modeling. The scattering in the experimental data thus may be attributed to the combined effect of contact friction and tip location. The contact friction may vary with local surface conditions for the indenter and the SiNLs, the tip location varies from test to test due to the lack of lateral resolution for exact positioning. Therefore, refined experiments with sufficient lateral resolution would reduce the data scattering and give a better measure of the friction properties. It is noted that the coefficients of friction used in the present study are about one order of magnitude lower than those obtained from a tribological test using a spherical diamond tip (tip radius 20 μm) on single-crystal Si (100) wafers [32]. The indentation tests on the SiNLs may offer a new approach to studying friction at the nanoscales.

4.4. Effect of elastic substrate

In the FE simulations discussed above, the SiNLs have been assumed to be supported by a rigid foundation. Consideration of an elastic substrate requires a significant increase in the number of FE elements and the computational time. To illustrate the effect of the elastic substrate, a FE model is constructed with six lines under a symmetric loading at the trench center. The dimensions of the substrate are 490 nm (height) by 900 nm (width) by 3000 nm (length). The material properties for the substrate are the same as those for the SiNLs, with Young's modulus 140 GPa and Poisson's ratio 0.27. The contact surface is defined as frictionless for this case. Figure 12 compares the load-displacement curves from the models with the elastic and rigid substrates. Clearly, the model with the elastic substrate is more compliant, and the critical load for the onset of instability is lower. A higher Young's modulus could be used in the FE model with an elastic substrate to match the load-displacement curve with

the experimental data, which would also increase the critical load. The final result for the critical load would be close to that of the rigid substrate model.

The stress distribution after the buckling transition, obtained from the FE model with the elastic substrate, is shown in Figure 13. As expected, stress concentration near the roots of the SiNLs is observed. In addition, relatively tensile high stresses in the direction parallel to the SiNLs exist at the top of center line, due to the localized buckling deformation. The locations of high tensile stresses, along with the specific crystal orientation and cleavage planes, would be useful for understanding fracture of the SiNLs observed in the experiments (see Figure 3).

5. SUMMARY

A buckling instability is observed in the nanoindentation tests of the parallel silicon nanolines. A systematic analysis of the buckling modes is presented based on finite element modeling. In particular, the effects of indenter tip location and contact friction on the critical load are discussed as possible causes for the scattering of the experimental data. The result from the present study demonstrates a potential methodology to study buckling, friction, and fracture at the nanoscale via a combination of experiments and modeling.

ACKNOWLEDGMENTS

The authors are grateful for the financial support by National Science Foundation through Grant no. CMMI-0654105. The work was performed in part at the Microelectronics Research Center of the University of Texas at Austin, a member of the National Nanofabrication Infrastructure Network supported by National Science Foundation under Award no. 0335765.

REFERENCES

[1] T. Namazu, Y. Isono, and T. Tanaka, "Evaluation of size effect on mechanical properties of single crystal silicon by nanoscale bending test using AFM," *Journal of Microelectromechanical Systems*, vol. 9, no. 4, pp. 450–459, 2000.

[2] T. Namazu, Y. Isono, and T. Tanaka, "Plastic deformation of nanometric single crystal silicon wire in AFM bending test at intermediate temperatures," *Journal of Microelectromechanical Systems*, vol. 11, no. 2, pp. 125–135, 2002.

[3] M. S. Islam, S. Sharma, T. I. Kamins, and R. S. Williams, "A novel interconnection technique for manufacturing nanowire devices," *Applied Physics A*, vol. 80, no. 6, pp. 1133–1140, 2005.

[4] M. Tabib-Azar, M. Nassirou, R. Wang, et al., "Mechanical properties of self-welded silicon nanobridges," *Applied Physics Letters*, vol. 87, no. 11, Article ID 113102, 3 pages, 2005.

[5] S. Hoffmann, I. Utke, B. Moser, et al., "Measurement of the bending strength of vapor-liquid-solid grown silicon nanowires," *Nano Letters*, vol. 6, no. 4, pp. 622–625, 2006.

[6] T. Alan, M. A. Hines, and A. T. Zehnder, "Effect of surface morphology on the fracture strength of silicon nanobeams," *Applied Physics Letters*, vol. 89, no. 9, Article ID 091901, 3 pages, 2006.

[7] J. Deneen, W. M. Mook, A. Minor, W. W. Gerberich, and C. B. Carter, "In situ deformation of silicon nanospheres," *Journal of Materials Science*, vol. 41, no. 14, pp. 4477–4483, 2006.

[8] R. He and P. Yang, "Giant piezoresistance effect in silicon nanowires," *Nature Nanotechnology*, vol. 1, no. 1, pp. 42–46, 2006.

[9] X. L. Feng, R. He, P. Yang, and M. L. Roukes, "Very high frequency silicon nanowire electromechanical resonators," *Nano Letters*, vol. 7, no. 7, pp. 1953–1959, 2007.

[10] M.-F. Yu, O. Lourie, M. J. Dyer, K. Moloni, T. F. Kelly, and R. S. Ruoff, "Strength and breaking mechanism of multiwalled carbon nanotubes under tensile load," *Science*, vol. 287, no. 5453, pp. 637–640, 2000.

[11] Y. Zhu and H. D. Espinosa, "An electromechanical material testing system for in situ electron microscopy and applications," *Proceedings of the National Academy of Sciences of the United States of America*, vol. 102, no. 41, pp. 14503–14508, 2005.

[12] J. Y. Huang, S. Chen, Z. F. Ren, et al., "Enhanced ductile behavior of tensile-elongated individual double-walled and triple-walled carbon nanotubes at high temperatures," *Physical Review Letters*, vol. 98, no. 18, Article ID 185501, 4 pages, 2007.

[13] M. M. J. Treacy, T. W. Ebbesen, and J. M. Gibson, "Exceptionally high Young's modulus observed for individual carbon nanotubes," *Nature*, vol. 381, no. 6584, pp. 678–680, 1996.

[14] P. Poncharal, Z. L. Wang, D. Ugarte, and W. A. de Heer, "Electrostatic deflections and electromechanical resonances of carbon nanotubes," *Science*, vol. 283, no. 5407, pp. 1513–1516, 1999.

[15] X. Li, B. Bhushan, K. Takashima, C.-W. Baek, and Y.-K. Kim, "Mechanical characterization of micro/nanoscale structures for MEMS/NEMS applications using nanoindentation techniques," *Ultramicroscopy*, vol. 97, no. 1–4, pp. 481–494, 2003.

[16] W. C. Oliver and G. M. Pharr, "An improved technique for determining hardness and elastic modulus using load and displacement sensing indentation experiments," *Journal of Materials Research*, vol. 7, no. 6, pp. 1564–1583, 1992.

[17] R. F. Cook, "Strength and sharp contact fracture of silicon," *Journal of Materials Science*, vol. 41, no. 3, pp. 841–872, 2006.

[18] M.-F. Yu, T. Kowalewski, and R. S. Ruoff, "Investigation of the radial deformability of individual carbon nanotubes under controlled indentation force," *Physical Review Letters*, vol. 85, no. 7, pp. 1456–1459, 2000.

[19] H. J. Qi, K. B. K. Teo, K. K. S. Lau, et al., "Determination of mechanical properties of carbon nanotubes and vertically aligned carbon nanotube forests using nanoindentation," *Journal of the Mechanics and Physics of Solids*, vol. 51, no. 11-12, pp. 2213–2237, 2003.

[20] X. Li, H. Gao, C. J. Murphy, and K. K. Caswell, "Nanoindentation of silver nanowires," *Nano Letters*, vol. 3, no. 11, pp. 1495–1498, 2003.

[21] G. Feng, W. D. Nix, Y. Yoon, and C. J. Lee, "A study of the mechanical properties of nanowires using nanoindentation," *Journal of Applied Physics*, vol. 99, no. 7, Article ID 074304, 10 pages, 2006.

[22] S. X. Mao, M. Zhao, and Z. L. Wang, "Nanoscale mechanical behavior of individual semiconducting nanobelts," *Applied Physics Letters*, vol. 83, no. 5, pp. 993–995, 2003.

[23] X. Chen, N. Ogasawara, M. Zhao, and N. Chiba, "On the uniqueness of measuring elastoplastic properties from indentation: the indistinguishable mystical materials," *Journal of the Mechanics and Physics of Solids*, vol. 55, no. 8, pp. 1618–1660, 2007.

[24] J. Li, K. J. Van Vliet, T. Zhu, S. Yip, and S. Suresh, "Atomistic mechanisms governing elastic limit and incipient plasticity in crystals," *Nature*, vol. 418, no. 6895, pp. 307–310, 2002.

[25] R. A. Allen, B. A. am Ende, M. W. Cresswell, et al., "Test structures for referencing electrical linewidth measurements to silicon lattice parameters using HRTEM," *IEEE Transactions on Semiconductor Manufacturing*, vol. 16, no. 2, pp. 239–248, 2003.

[26] B. Li, M. K. Kang, K. Lu, et al., "Fabrication and characterization of patterned single-crystal silicon nanolines," *Nano Letters*, vol. 8, no. 1, pp. 92–98, 2008.

[27] J. J. Vlassak, M. Ciavarella, J. R. Barber, and X. Wang, "The indentation modulus of elastically anisotropic materials for indenters of arbitrary shape," *Journal of the Mechanics and Physics of Solids*, vol. 51, no. 9, pp. 1701–1721, 2003.

[28] X. Chen, J. W. Hutchinson, and A. G. Evans, "Simulation of the high temperature impression of thermal barrier coatings with columnar microstructure," *Acta Materialia*, vol. 52, no. 3, pp. 565–571, 2004.

[29] M. Watanabe, T. Xu, C. G. Levi, A. S. Gandhi, and A. G. Evans, "Shear band formation in columnar thermal barrier oxides," *Acta Materialia*, vol. 53, no. 13, pp. 3765–3773, 2005.

[30] "ABAQUS Documentation (Version 6.6)," ABAQUS, Inc., Providence, RI, USA, 2006.

[31] E. Riks, "An incremental approach to the solution of snapping and buckling problems," *International Journal of Solids and Structures*, vol. 15, no. 7, pp. 529–551, 1979.

[32] B. Bhushan and X. Li, "Micromechanical and tribological characterization of doped single-crystal silicon and polysilicon films for microelectromechanical systems devices," *Journal of Materials Research*, vol. 12, no. 1, pp. 54–63, 1997.

Research Letters in Materials Science

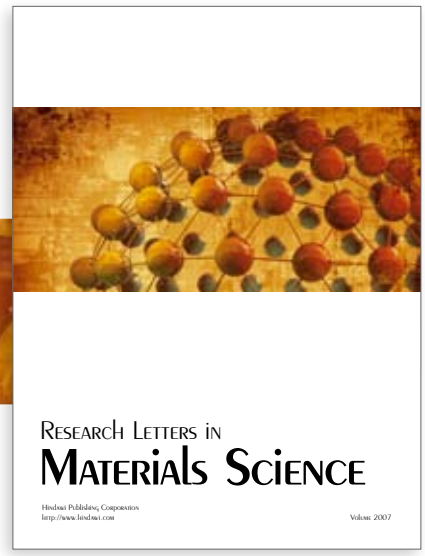

Why publish in this journal?

Research Letters in Materials Science is devoted to very fast publication of short, high-quality manuscripts in the broad field of materials science. Manuscripts should not exceed 4 pages in their final published form. Average time from submission to publication shall be around 60 days.

Why publish in this journal?

Wide Dissemination

All articles published in the journal are freely available online with no subscription or registration barriers. Every interested reader can download, print, read, and cite your article

Quick Publication

The journal employs an online "Manuscript Tracking System" which helps streamline and speed the peer review so all manuscripts receive fast and rigorous peer review. Accepted articles appear online as soon as they are accepted, and shortly after the final published version is released online following a thorough in-house production process.

Professional Publishing Services

The journal provides professional copyediting, typesetting, graphics, editing, and reference validation to all accepted manuscripts.

Keeping Your Copyright

Authors retain the copyright of their manuscript, which are published using the "Creative Commons Attribution License," which permits unrestricted use of all published material provided that it is properly cited.

Extensive Indexing

Articles published in this journal will be indexed in several major indexing databases to ensure the maximum possible visibility of each published article.

Submit your Manuscript Now...

In order to submit your manuscript, please visit the journal's website that can be found at **http://www.hindawi.com/journals/rlms/** and click on the "Manuscript Submission" link in the navigational bar.

Should you need help or have any questions, please drop an email to the journal's editorial office at **rlms@hindawi.com**

ISSN: 1687-6822; e-ISSN: 1687-6830; doi:10.1155/RLMS

Hindawi Publishing Corporation
410 Park Avenue, 15th Floor, #287 pmb, New York, NY 10022, USA
HINDAWI

Editorial Board
Reza Abbaschian, USA
Robert S. Averback, USA
Kwai S. Chan, USA
D. Chen, Canada
Stephen C. Danforth, USA
Chapal Kumar Das, India
Chris H. J. Davies, Australia
Seshu Babu Desu, USA
J. G. Ekerdt, USA
Raymond W. Flumerfelt, USA
Easo P. George, USA
Emmanuel P. Giannelis, USA
Jack Gillespie, USA
Jeffrey T. Glass, USA
Hiroki Habazaki, Japan
Chun-Hway Hsueh, USA
Xiaozhi Hu, Australia
Shyh-Chin Huang, Taiwan
Hamlin Jennings, USA
S. Komar Kawatra, USA
Pearl Lee-Sullivan, Canada
Pavel Lejcek, Czech Republic
Markku Leskela, Finland
Maria Antonietta Loi,
The Netherlands
G. Q. Lu, Australia
Yiu-Wing Mai, Australia
Peter Majewski, Australia
Shuichi Miyazaki, Japan
Zuhair Munir, USA
Luigi Nicolais, Italy
Tsutomu Ohzuku, Japan
J. Michael Rigsbee, USA
Jainagesh A. Sekhar, USA
Steven L. Suib, USA
George E. Totten, USA
An Pang Tsai, Japan
Rui Vilar, Portugal
H. Daniel Wagner, Israel
K. Xia, Australia
Jenn-Ming Yang, USA
Yadong Yin, USA
Dao Hua Zhang, Singapore